PHYSICAL REVIEW D

PARTICLES AND FIELDS

THIRD SERIES, VOL. 3, NO. 1 — 1 JANUARY 1971

Proton-Proton Differential Cross Sections from 600 to 1800 MeV/c*

B. A. RYAN† AND A. KANOFSKY
Lehigh University, Bethlehem, Pennsylvania 18015

AND

T. J. DEVLIN,‡ R. E. MISCHKE, AND P. F. SHEPARD§
Princeton University, Princeton, New Jersey 08540

(Received 17 September 1970)

Proton-proton elastic differential cross sections have been measured for incident laboratory momenta of 600–1800 MeV/c and c.m. angles of 5°–90°. The data span, in a single experiment, the intermediate energy region from isotropic differential cross sections at lower energies to the development of a clear diffraction peak at higher energies. Parameters for phenomenological formulations derived from the experimental results are presented.

I. INTRODUCTION

PROTON-PROTON elastic scattering has been measured at the 3-GeV Princeton-Pennsylvania Accelerator (PPA) for incident laboratory momenta of 600–1800 MeV/c and c.m. angles of 5°–90°. The experiment covers a momentum and angular range which exhibits many of the significant characteristics of proton-proton scattering. The differential cross section is virtually isotropic at lower momenta. At higher momenta a forward diffraction peak develops; its amplitude increases with momentum. The cross sections are flat at 90° c.m., as required by identical-particle symmetry.

This experiment forms part of a more general nucleon-nucleon scattering program in which these data can be combined with n-p data taken with the same experimental configuration.[1] Previous experimental data which overlap our momentum region have been summarized by several authors.[2–6] Theoretical treatments of p-p scattering are usually confined to lower energies, as in the phase-shift analysis of MacGregor, Arndt, and Wright,[6] or to very-high-energy Regge-type theories.

II. APPARATUS AND EXPERIMENTAL PROCEDURES

The experiment was set up in the 34° beam line of the PPA with a liquid-hydrogen target located 108 ft from the internal production target (see Fig. 1). Collimators were located at 70 and 90 ft from the internal target, and final beam definition was accomplished by a 1-in.×1-in. scintillation counter ($B4$). Vacuum pipe was installed for 45% of the length of the beam line. Particle momentum was determined by time-of-flight (TOF) techniques. The transition from the p-p to the n-p phase of the experiment was accomplished by turning on sweeping magnets to remove all charged particles.[7]

The liquid-hydrogen target was 14 in. long and 2 in. in diam [2.5 g/cm^2 of liquid H_2 (LH_2)]. Protons scat-

---

* Work supported in part by the U. S. Atomic Energy Commission under Contract No. AT(30-1)-4159.

† National Aeronautics and Space Administration Trainee. Present address: International Business Machines, East Fishkill, N. Y.

‡ Present address: Rutgers–The State University, New Brunswick, N. J. Supported in part by the National Science Foundation under Grant No. GU-1592.

§ Present address: University of California, Los Angeles, Calif.

[1] R. E. Mischke, P. F. Shepard, and Thomas J. Devlin, Phys. Rev. Letters **23**, 542 (1969); P. F. Shepard, T. J. Devlin, R. E. Mischke, and J. Solomon, Princeton-Pennsylvania Accelerator Report No. PPAR-10, Princeton, N. J., 1969 (unpublished).

[2] R. Wilson, *The Nucleon-Nucleon Interaction* (Interscience, New York, 1963).

[3] W. N. Hess, Rev. Mod. Phys. **30**, 364 (1958).

[4] H. A. Stoddart and B. J. Wilson, Atomic Energy Research Establishment Report No. AERE-Bib. 135, 1961 (unpublished).

[5] J. L. Hall, Atomic Energy Research Establishment Report No. AERE-149, 1966 (unpublished).

[6] M. H. MacGregor, R. A. Arndt, and R. M. Wright, Phys. Rev. **169**, 1149 (1968).

[7] We thank Professor J. Cronin for first suggesting that we perform both experiments in the same beam.

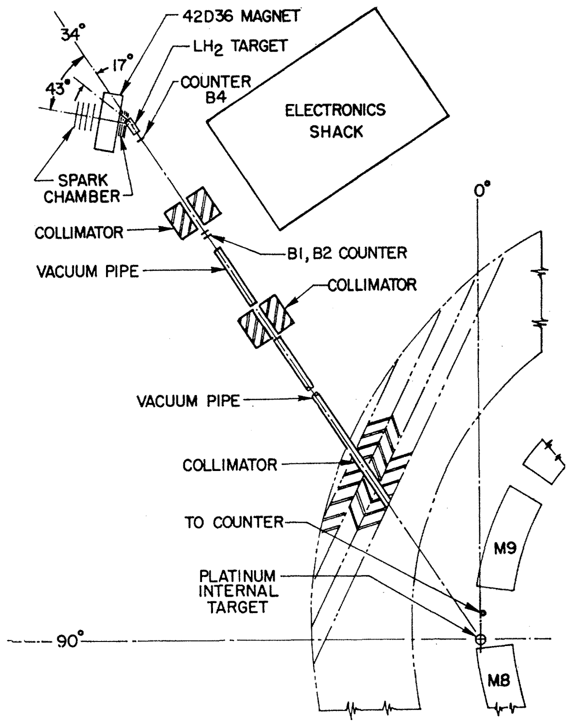

FIG. 1. Schematic plan view of the experimental arrangement. The spectrometer is shown in the wide-angle configuration. For clarity, a large midsection of the beam line and some of the shielding have been omitted.

tered from the LH_2 target were detected in a wire-spark-chamber spectrometer (see Fig. 2). The spectrometer magnet was 36 in.×40 in. with a 10-in. gap. The field was maintained at 7.45 kG. Four wire-chamber gaps were placed on each side of the magnet. They were constructed of 0.007-in. copper wire wound on a $\frac{3}{8}$-in. epoxy-fiberglass frame with ~1-mm wire spacing. The four front chambers had active areas of 10 in.×30 in. and were spaced at $1\frac{1}{2}$-in. intervals. The four rear chambers had active areas of 16 in.×50 in. and were spaced at 8-in. intervals. The second and third chambers in the front (rear) had their coordinate systems rotated by 45° (30°) from the vertical in order to resolve stereo ambiguities. The active volume of each gap was enclosed by 0.002-in. Mylar windows and filled with He gas.

Data were taken with the spectrometer positioned at angles of 17° and 43° with respect to the beam. The spectrometer polarity was reversed in both positions, giving four partially overlapping scattering-angle ranges. The first (range A: 0–15° lab) was used for calibration; the second (range B: 10°–30° lab) and third (range C: 20°–45° lab) produced cross-section data; and the fourth was redundant since it corresponded to c.m. scattering angles greater than 90°. Figure 3 gives the angular acceptance versus momentum for ranges B and C.

In addition to protons, the incident beam contained other charged and neutral particles. The neutral particles could not trigger the incident beam telescope (see Fig. 1). Most of the charged contaminants had a much higher velocity than the heavier protons and were separated on the basis of their TOF. All but a few of the remaining slow pions decay; slow electrons are stopped by the material in the beam, and muons do not interact strongly. For the TOF intervals used, the beam was experimentally determined to be better than 99% protons, in agreement with prior estimates based on beam surveys.[8]

The use of TOF to determine the momenta of incident protons is made possible by the tightly bunched beam spill structure at the PPA. The internal beam bunches (buckets) struck the production target every 67 nsec and triggered a glycerin Čerenkov counter (T_0) placed near the internal target. Particles arriving at counter $B4$, located in our beam line 105 ft from the internal target, were timed with respect to T_0. With a time resolution of 2-nsec full width at half-maximum, the momentum resolution was 0.25% at 600 MeV/c and 2.5% at 1800 MeV/c. An ambiguity in the TOF exists since a slow particle can be overtaken by a fast particle from the next bucket. It was resolved by the use of a second TOF system made up of T_0 and a counter $B1$ located at an intermediate point 87 ft from the production target.

Scattered protons or other charged particles emerging from the target were detected by the counter P_1 in front of the magnet and the P_2, P_3 array behind the rear chambers. Anti-counters (A_1–A_3) were placed at the exit aperture of the magnet to eliminate particles scattering from the magnet steel. In range B, a beam veto counter, $B5$, eliminated unscattered particles. The locations of the counters are shown in Fig. 2 and a schematic of the event logic is presented in Fig. 4.

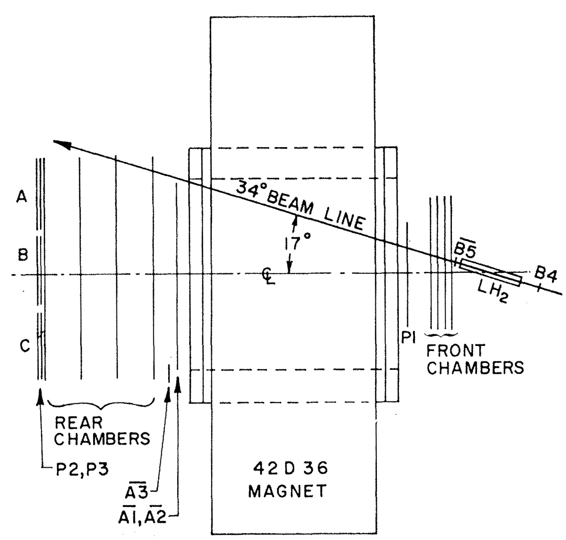

FIG. 2. Plan view of the wire-spark-chamber spectrometer in the narrow-angle configuration.

[8] P. A. Piroué and A. J. S. Smith, Phys. Rev. 148, 1315 (1966).

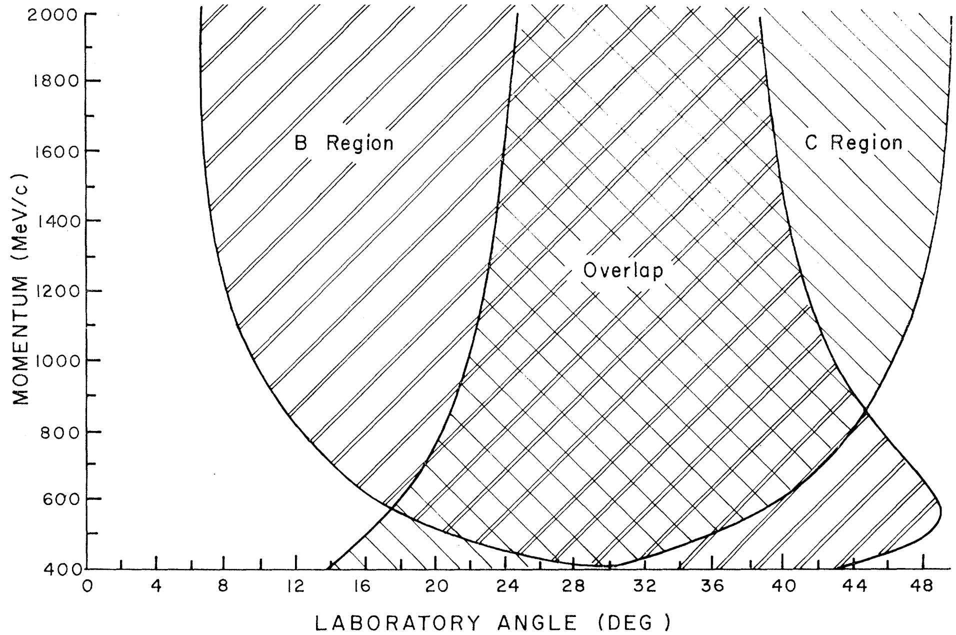

FIG. 3. Angular acceptance of the spectrometer. At any given incident proton momentum (vertical scale) the spectrometer accepted elastic events over a range of laboratory polar scattering angles between the indicated limits.

When a scattered particle was detected in coincidence with an incident particle, the spark chambers were fired. The information from each magnetostrictive delay line and the TOF data were accepted by an on-line computer for editing, processing, and permanent storage on magnetic tape. A primary task of the computer was the buffering of randomly occurring events to maximize the efficiency of the slow tape-writing device. The programs compressed the data for each event to about one-half their original length.

Each event was processed on-line by spatial reconstruction of the spark locations and straight-line track fitting on each side of the magnet. From this the momentum of the scattered particle was computed. It was combined with the energy of the incident proton based on its TOF to calculate the invariant mass of the recoiling system assuming *p-p* scattering.

Elastic events were identified during the data collection period through computer-generated displays of the invariant-mass histograms. Other displays such as TOF

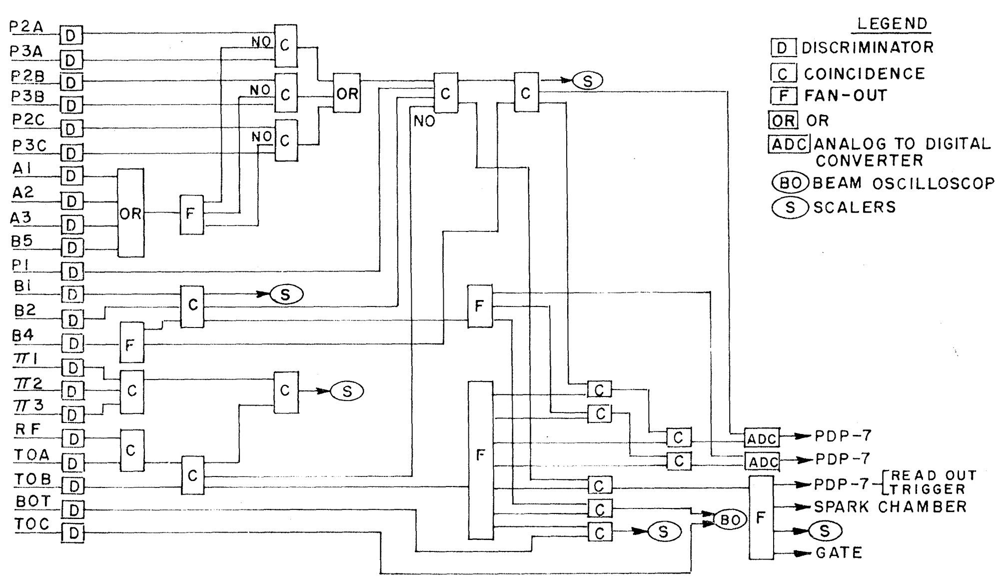

FIG. 4. Block diagram of the event trigger logic. The function of most counters is explained in the text and their locations are shown in Figs. 1 and 2. BOT and $\pi_1\pi_2\pi_3$ were monitors of the number of primary protons striking the production target. RF, a synchrotron master oscillator signal, T_{0A} and T_{0B} were used to generate the TOF reference signal. A similar signal, T_{0C}, was used for oscilloscope display.

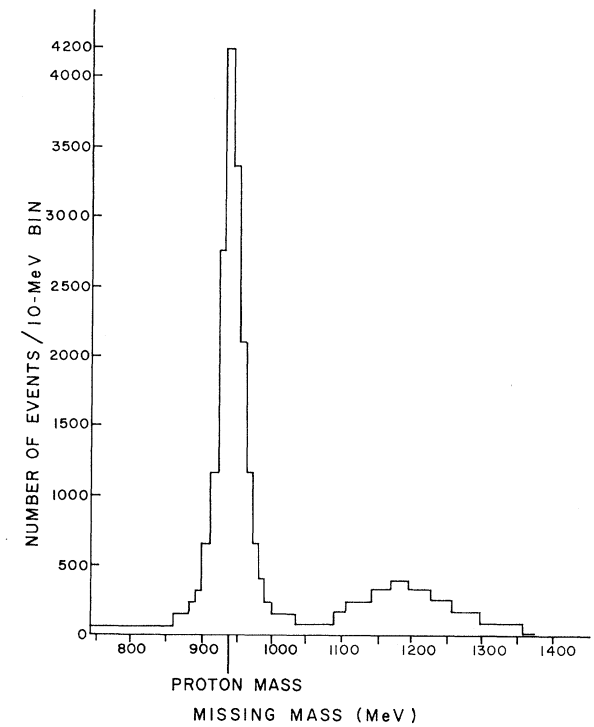

FIG. 5. Missing mass assuming the reaction $p+p \to p+X$. The elastic scattering peak is evident, as is inelastic production starting one pion mass above the proton mass.

distributions and delay line performance were valuable monitors of the experiment. Bookkeeping and monitoring functions were also performed by the computer.[9]

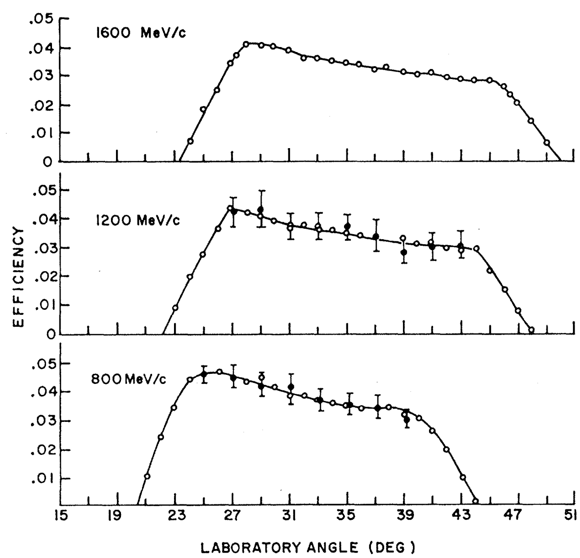

FIG. 6. Examples of geometric efficiency graphs. The open circles represent the results of a Monte Carlo calculation. The closed circles with error bars represent calculations made from the data themselves. The statistical accuracy of the data at the highest energy was not sufficient to allow a direct measurement of geometric efficiency.

[9] R. E. Mischke, J. Metzger, P. F. Shepard, and T. J. Devlin, Princeton-Pennsylvania Accelerator Report No. PPAR-3, Princeton, N. J., 1968 (unpublished).

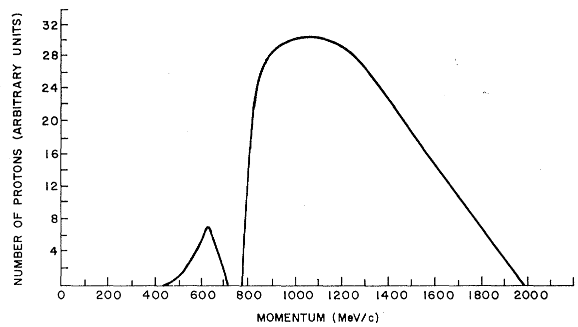

FIG. 7. Momentum spectrum for incident protons. This is not a true production spectrum for the synchrotron; it has many features imposed by our beam and triggering system. The shape of the high-energy portion and the gap at 750 MeV/c are imposed by TOF veto on fast particles. The absence of low-energy protons is due to multiple Coulomb scattering and bias in our "ghost" reclaiming procedure.

III. DATA ANALYSIS AND RESULTS

Since the on-line analysis made several approximations for speed and simplicity, a more sophisticated off-line analysis was carried out. After the real-space locations of the sparks were determined and straight lines were fitted in both horizontal and vertical planes for both sets of chambers, the momentum of the scattered particle was calculated by an iterative method which included vertical focusing corrections. The trajectory was extrapolated back to the target and the scattering angles were evaluated.

When the energy of the incident particle was computed from its TOF, a correction for ionization losses along its path length was applied. The correction varied from 2.0% at 600 MeV/c to 0.1% at 1800 MeV/c. Corrections for energy loss of the incident and recoil proton in the target varied from a maximum value of 9% for a 600-MeV/c proton going through all 14 in. of LH_2 to less than 0.6% for an 1800-MeV/c proton. Most detected particles went through less than the full target length. The energy loss due to the material in the spectrometer was 1.2% at 600 MeV/c and 0.1% at 1800 MeV/c.

TABLE I. Disposition of events during the data analysis.

Total No. of events	*B* range 86 860	*C* range 45 340
Physical reconstruction cuts		
Not enough sparks	30 048	1518
No track found	8746	3110
Negative momentum	14 222	123
More than one track	1672	458
Others	202	214
No. surviving physical reconstruction	31 970	39 917
Kinematical reconstruction cuts		
χ^2 tests	1860	1450
*B*5 Anti-counter	2170	0
Solid-angle limits	4941	11 565
Missing-mass test	6030	7029
Others	1735	2357
No. of elastic events used to calculate cross sections	15 222	17 508

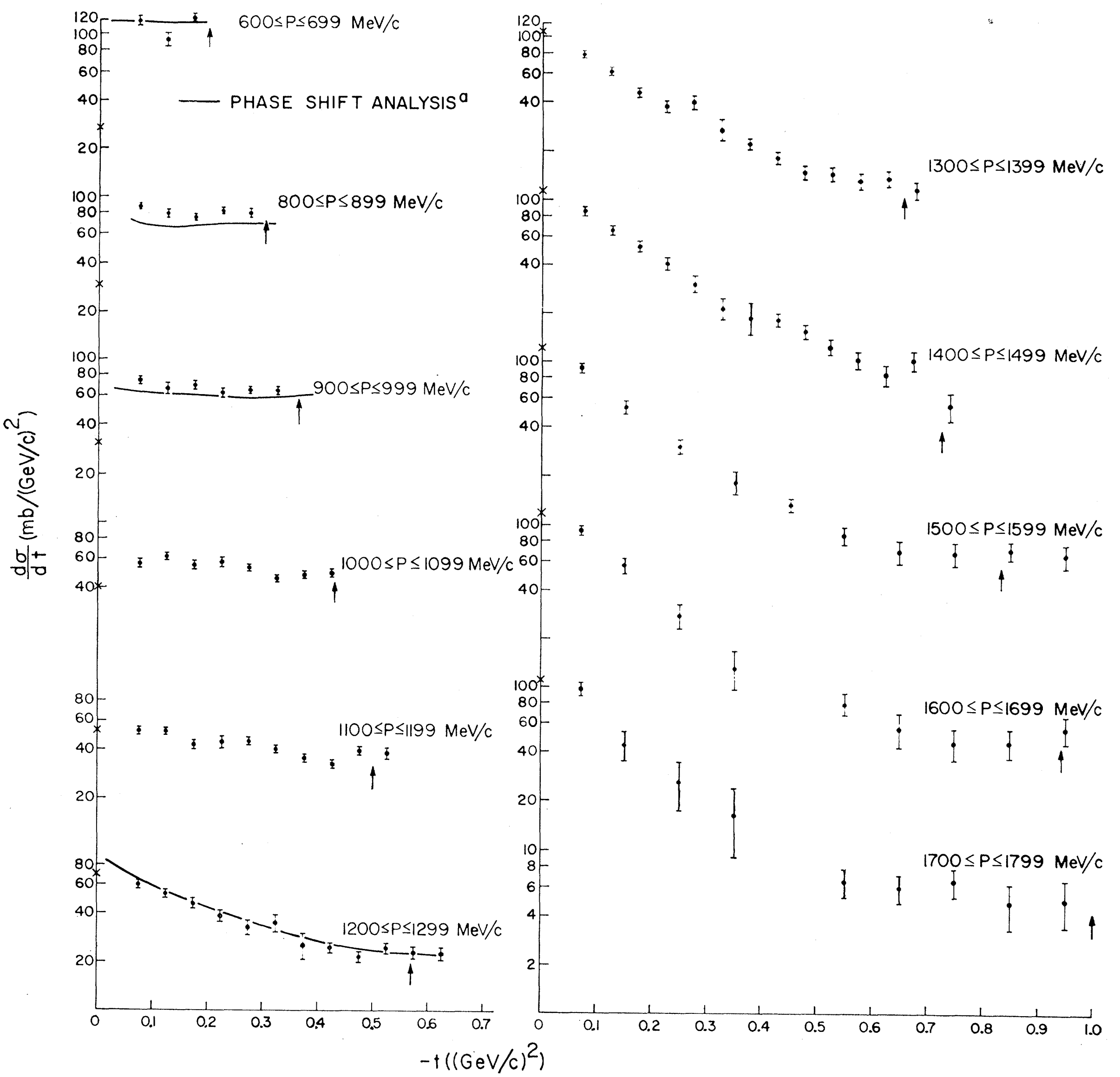

FIG. 8. Normalized differential cross sections from 600 to 1800 MeV/c. The points on the vertical axes are $d\sigma/dt$ at $t=0$ obtained from the optical theorem. The arrows indicate 90° (c.m.) at the central momentum in each bin. (a) The solid curves are from the Livermore phase-shift solutions at 668, 875, 981, and 1281 MeV/c; see Ref. 10.

It was assumed that the incident and scattered particles were protons and the missing mass for each event was calculated. Figure 5 shows the missing-mass distribution for the C data. The peak at the proton mass is due to elastically scattered events. The four-momentum transfer t was computed for each event in the elastic peak and the events were binned by incident momentum (P) and momentum transfer (t). Each event was corrected for spark-chamber efficiency and solid-angle acceptance.

The solid-angle correction factor was determined in two ways and the answers were compared for consistency. A Monte Carlo program simulated the experimental geometry and randomly generated events from the target for a fixed incident momentum and polar scattering angle. Ionization corrections were included and the fraction of events passing through the active volume of the spectrometer was recorded. Also the angular acceptance was computed from the data by binning all the elastic events according to incident momentum, polar angle, and azimuthal scattering angle. The fraction of azimuthal scattering angles populated by the data gave excellent agreement with the Monte Carlo result. Figure 6 shows typical solid-angle acceptance for the C region. The open circles joined by the solid curves are the Monte Carlo results. The closed circles are derived from the data. Note that the "linear" region is nearly independent of energy.

The chamber efficiency was determined from the data by hypothetically dividing all eight chambers into 1-in.

TABLE II. Proton-proton elastic differential cross sections.

P_{inc}(lab) (MeV/c)	T_{inc}(lab) (MeV)	$\lvert t\rvert$ (GeV/c)^2	$d\sigma/dt$ [mb/(GeV/c)^2]	$\theta_{\mathrm{c.m.}}$ (deg)	$\cos\theta_{\mathrm{c.m.}}$	$d\sigma/d\Omega$ (mb/sr)	Systematic uncertainty (%)
600–699	175.5–231.8	0.05–0.999	122.5±7.5	52.66	0.607	3.72±0.23	5.4
		0.10–0.149	95.4±8.3	69.87	0.344	2.89±0.25	
		0.15–0.199	128.3±6.3	85.30	0.082	3.89±0.19	
800–899	294.8–361.2	0.05–0.099	89.5±4.0	40.88	0.756	4.38±0.20	2.9
		0.10–0.149	80.7±4.5	53.59	0.594	3.95±0.22	
		0.15–0.199	76.6±3.2	64.47	0.431	3.75±0.16	
		0.20–0.249	84.3±3.7	74.43	0.268	4.13±0.18	
		0.25–0.299	81.8±4.9	83.93	0.106	4.00±0.24	
900–999	361.9–432.3	0.05–0.099	76.1±3.8	37.00	0.799	4.51±0.23	3.0
		0.10–0.149	67.8±5.3	48.36	0.664	4.02±0.32	
		0.15–0.199	71.2±4.2	57.99	0.530	4.22±0.25	
		0.20–0.249	63.9±3.9	66.68	0.396	3.79±0.23	
		0.25–0.299	66.6±2.8	74.83	0.262	3.95±0.17	
		0.30–0.349	66.3±3.2	82.68	0.127	3.93±0.19	
1000–1099	433.0–506.8	0.05–0.099	58.1±2.9	33.91	0.830	4.08±0.21	3.4
		0.10–0.149	63.6±3.3	44.24	0.716	4.46±0.23	
		0.15–0.199	56.5±3.5	52.91	0.603	3.97±0.25	
		0.20–0.249	58.6±3.7	60.68	0.490	4.11±0.26	
		0.25–0.299	54.4±2.4	67.90	0.376	3.82±0.17	
		0.30–0.349	46.9±2.3	74.76	0.263	3.29±0.16	
		0.35–0.399	49.5±2.6	81.41	0.149	3.47±0.18	
		0.40–0.449	50.9±3.0	87.94	0.036	3.57±0.21	
1100–1199	507.6–584.2	0.05–0.099	53.3±2.8	31.40	0 854	4.35±0.23	3.5
		0.10–0.149	52.7±2.8	40.89	0.756	4.30±0.23	
		0.15–0.199	43.7±2.8	48.83	0.658	3.56±0.23	
		0.20–0.249	45.1±3.6	55.89	0.561	3.68±0.29	
		0.25–0.299	46.1±2.5	62.41	0.463	3.76±0.20	
		0.30–0.349	41.4±2.1	68.56	0.366	3.37±0.17	
		0.35–0.399	36.3±2.0	74.46	0.268	2.96±0.17	
		0.40–0.449	33.6±2.0	80.20	0.170	2.74±0.17	
		0.45–0.499	40.4±2.4	85.83	0.073	3.29±0.20	
		0.50–0.549	38.9±2.9	91.43	−0.025	3.17±0.24	
1200–1299	585.0–664.2	0.05–0.099	62.2±3.7	29.30	0.872	5.80±0.34	3.7
		0.10–0.149	54.1±3.3	38.12	0.787	5.04±0.30	
		0.15–0.199	47.2±3.2	45.46	0.701	4.41±0.30	
		0.20–0.249	39.7±3.1	51.97	0.616	3.70±0.29	
		0.25–0.299	33.9±3.4	57.94	0.531	3.16±0.32	
		0.30–0.349	36.0±4.2	63.54	0.445	3.35±0.39	
		0.35–0.399	26.4±4.6	68.89	0.360	2.46±0.43	
		0.40–0.449	25.5±1.7	74.04	0.275	2.38±0.16	
		0.45–0.499	22.4±1.7	79.07	0.190	2.09±0.16	
		0.50–0.549	25.2±1.8	84.01	0.104	2.35±0.17	
		0.55–0.599	24.0±1.9	88.91	0.019	2.24±0.18	
		0.60–0 .649	24.1±1.4	93.80	−0.066	2.25±0.13	
1300–1399	665.0–746.3	0.05–0.099	80.6±3.9	27.53	0.887	8.49±0.42	4.3
		0.10–0.149	63.8±3.7	35.78	0.811	6.72±0.39	
		0.15–0.199	46.6±3.2	42.63	0.736	4.92±0.34	
		0.20–0.249	38.6±3.2	48.68	0.660	4.07±0.33	
		0.25–0.299	40.8±3.7	54.22	0.585	4.30±0.39	
		0.30–0.349	28.0±4.1	59.39	0.509	2.96±0.43	
		0.35–0.399	23.0±1.7	64.30	0.434	2.42±0.17	
		0.40–0.449	18.8±1.5	69.01	0.358	1.98±0.16	
		0.45–0.499	15.3±1.4	73.58	0.283	1.61±0.15	
		0.50–0.549	15.1±1.4	78.04	0.207	1.59±0.15	
		0.55–0.599	13.5±1.4	82.43	0.132	1.42±0.15	
		0.60–0.649	14.0±1.5	86.78	0.056	1.48±0.16	
		0.65–0.699	11.8±1.4	91.11	−0.019	1.25±0.15	
1400–1499	747.1–830.2	0.05–0.099	89.1±5.0	26.02	0.899	10.50±0.59	4.9
		0.10–0.149	68.5±4.3	33.79	0.831	8.06±0.51	
		0.15–0.199	54.6±4.0	40.22	0.764	6.43±0.47	
		0 20–0.249	42.7±3.6	45.89	0.696	5.03±0.42	
		0.25–0.299	32.1±3.6	51.07	0.628	3.78±0.42	
		0.30–0.349	22.6±3.3	55.88	0.561	2.66±0.39	
		0.35–0.399	19.8±4.5	60.44	0.493	2.34±0.53	
		0.40–0.449	19.3±1.7	64.80	0.426	2.27±0.20	
		0.45–0.499	16.4±1.5	69.01	0.358	1.94±0.18	

TABLE II. (*Continued*)

P_{inc}(lab) (MeV/c)	T_{inc}(lab) (MeV)	$\|t\|$ (GeV/c)^2	$d\sigma/dt$ [mb/(GeV/c)^2]	$\theta_{c.m.}$ (deg)	$\cos\theta_{c.m.}$	$d\sigma/d\Omega$ (mb/sr)	Systematic uncertainty (%)
1400–1499	747.1–830.2	0.50–0.549	12.7±1.4	73.10	0.291	1.50±0.16	
		0.55–0.599	10.5±1.3	77.11	0.223	1.24±0.15	
		0.60–0.649	8.5±1.2	81.05	0.156	1.01±0.14	
		0.65–0.699	10.4±1.4	84.95	0.088	1.23±0.16	
		0.70–0.749	5.5±1.1	88.83	0.020	0.65±0.13	
1500–1599	831.0–915.7	0.05–0.099	93.5±5.5	24.70	0.908	12.19±0.72	5.3
		0.10–0.199	55.3±4.9	35.22	0.817	7.21±0.64	
		0.20–0.299	31.6±3.1	45.97	0.695	4.13±0.40	
		0.30–0.399	19.3±2.9	55.04	0.573	2.51±0.38	
		0.40–0.499	14.0±1.3	63.19	0.451	1.83±0.17	
		0.50–0.599	8.8±1.1	70.79	0.329	1.15±0.14	
		0.60–0.699	7.0±1.1	78.06	0.207	0.91±0.14	
		0.70–0.799	6.8±1.1	85.13	0.085	0.88±0.14	
		0.80–0.899	7.1±0.9	92.12	−0.037	0.92±0.12	
		0.90–0.999	6.6±1.1	99.15	−0.159	0.86±0.14	
1600–1699	916.6–1002.6	0.05–0.099	93.8±6.2	23.55	0.917	13.44±0.89	5.6
		0.10–0.199	58.5±6.1	33.55	0.833	8.39±0.88	
		0.20–0.299	28.8±4.7	43.75	0.722	4.13±0.67	
		0.30–0.399	13.7±3.5	52.31	0.611	1.96±0.50	
		0.50–0.599	8.3±1.2	67.09	0.389	1.19±0.17	
		0.60–0.699	5.6±1.3	73.85	0.278	0.81±0.19	
		0.70–0.799	4.6±1.0	80.38	0.167	0.66±0.14	
		0.80–0.899	4.6±0.9	86.78	0.056	0.66±0.13	
		0.90–0.999	5.6±1.1	93.15	−0.055	0.81±0.16	
1700–1799	1003.5–1090.7	0.05–0.099	98.5±9.1	22.53	0.924	15.41±1.43	6.0
		0.10–0.199	46.0±8.9	32.07	0.847	7.19±1.39	
		0.20–0.299	27.2±8.7	41.79	0.746	4.25±1.36	
		0.30–0.399	16.9±7.7	49.92	0.644	2.64±1.20	
		0.50–0.599	6.8±1.3	63.88	0.440	1.06±0.20	
		0.60–0.699	6.2±1.2	70.21	0.339	0.98±0.19	
		0.70–0.799	6.5±1.3	76.30	0.237	1.01±0.20	
		0.80–0.899	4.8±1.5	82.24	0.135	0.75±0.23	
		0.90–0.999	5.0±1.6	88.09	0.033	0.78±0.25	

squares and using three-spark and four-spark events to determine whether or not the appropriate chambers and delay lines responded. In this manner the inefficiencies in the chambers and delay lines were established as a function of position. By examining all the possible ways a good event could take place, the probability of detecting that event was determined. These corrections were between 6 and 20% for the B data and between 0.8 and 5% for the C data.

Possible backgrounds were investigated by taking a target-empty run between each target-full run. When each trajectory was extrapolated back to a reference plane in the target, a position-distribution scatterplot showed that the major target-empty contribution was from events produced in the Mylar end windows. These could be eliminated from all the data by appropriate cuts. The remaining events were consistent with those expected from residual hydrogen gas (~1%); thus no target-empty subtraction was necessary.

The differential cross sections were calculated by dividing the corrected number of events in each P and t bin by the number of incident particles with the appropriate momentum. The momentum spectrum of incident protons was determined from the data taken in range A with the target empty and the spectrometer on. These data provided several checks on the performance of the system; the events used were unscattered protons as determined by a missing-mass test. This procedure eliminated all beam contaminants. Only 1.2% of these data had a value of $|t|$ greater than 0.005 (GeV/c)^2 and the missing-mass peak was within 0.4% of the proton mass. The momentum computed from the spectrometer was within 1% of the value computed by TOF.

The momentum spectrum for ranges A and C is shown in Fig. 7. The secondary peak is due to slow protons which were recovered by the dual TOF system. The gap is due to a timing window set to eliminate very fast particles with flight times near 107 nsec. It necessarily eliminated also those with flight times near 174 nsec, i.e., 107 nsec plus one RF period. During data collection in the B range the timing window was shifted, causing an inefficiency above 1300 MeV/c. The fraction of incident particles passed by the timing window decreased linearly from 100% at 1300 MeV/c to 10% at 1750 MeV/c. When appropriate corrections were made to the B-range data, the cross sections agreed with those from the C-range data where they overlapped.

The results are based on 86 860 events recorded in the B position and 45 340 events recorded in the C position. After all cuts, the number of events remaining was 15 222 in the B region and 17 508 in the C region. The

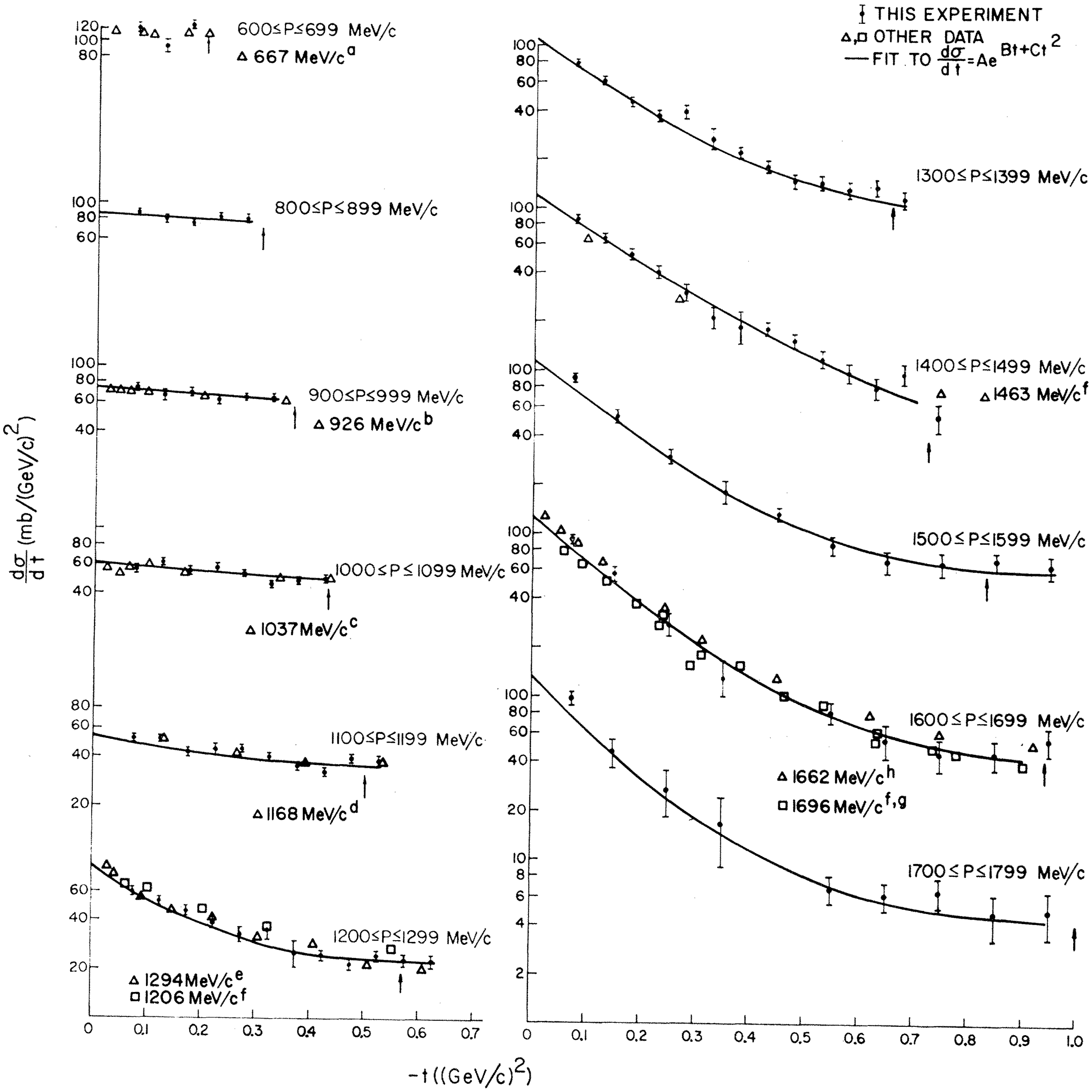

FIG. 9. Data from this experiment and other published data. The solid lines represent a fit to the data of the expression in Eq. (1). References to data from other experiments are given below. Most can be found in Wilson (Ref. 2). (a) J. Tinlot and R. E. Warner, Phys. Rev. **124**, 890 (1961); (b) J. R. Holt, J. C. Kluyver, and J. A. Moore, Proc. Phys. Soc. (London) **71**, 781 (1958); (c) Mescheryakov *et al.*, Dokl. Akad. Nauk SSSR **99**, 959 (1954); Bull. Acad. Sci. USSR, Phys. Ser. **19**, 548 (1955); see Ref. 2. (d) Selector *et al.*, Dokl. Akad. Nauk SSSR **99**, 967 (1954); see Ref. 2; (e) N. Bogachev and I. Vzorov, Dokl. Akad. Nauk SSSR **99**, 931 (1954); N. Bogachev, Dokl. Akad. Nauk SSSR **108**, 806 (1956) [Soviet Phys. Doklady **1**, 361 (1956)]; see Ref. 2; (f) L. M. Smith, A. W. McReynolds, and G. Snow, Phys. Rev. **97**, 1186 (1960); (g) J. D. Dowell, W. R. Frisken, G. Martelli, B. Musgrave, H. B. van der Raay, and R. Rubinstein, Nuovo Cimento **18**, 818 (1960); (h) W. K. MacFarlane, R. J. Hover, A. W. O'Dell, E. J. Sacharids, and G. H. Eaton, *ibid.* **23**, 690 (1962); **28**, 943 (1963).

disposition of events during the spatial and kinematical reconstruction is summarized in Table I.

The normalized differential cross sections are shown in Fig. 8 and listed in Table II. The errors shown are statistical only. Systematic uncertainties for each momentum (but which are uncorrelated between momenta) are given separately in the tables. The points on the vertical axis are $d\sigma/dt$ at $t=0$ as determined from the optical theorem (assuming a purely imaginary scattering amplitude) using total cross sections compiled from Refs. 2–5. The arrows indicate 90° c.m., midway in the indicated momentum range.

There does not seem to be an obvious choice of a best parametrization for these data. The solid lines in Fig. 8 represent the prediction of the Livermore phase-shift solution at the energies for which they have been

TABLE III. Fits to the data of the function $d\sigma/dt = Ae^{Bt+Ct^2}$.

P_{lab} (MeV/c)	A [mb/(GeV/c)^2]	B (GeV/c)$^{-2}$	C (GeV/c)$^{-4}$
800–899	87.1± 5.1	−0.96±0.55	2.91±1.81
900–999	78.8± 4.7	−1.17±0.57	1.89±1.69
1000–1099	64.7± 3.6	−1.00±0.52	0.72±1.31
1100–1199	60.4± 3.4	−2.01±0.47	2.10±0.99
1200–1299	79.6± 4.7	−4.38±0.44	3.96±0.72
1300–1399	107.4± 5.8	−5.76±0.41	3.68±0.69
1400–1499	116.1± 7.1	−5.45±0.46	2.04±0.79
1500–1599	126.2± 9.6	−6.51±0.34	3.56±0.39
1600–1699	137.0±11.7	−7.20±0.49	3.80±0.57
1700–1799	140.9±15.7	−7.66±0.59	4.39±0.72

evaluated.[10] Even though these cover only the lower half of our data, the number of free parameters to be specified is already greater than 30.

A frequently used phenomenological parametrization is

$$d\sigma/dt = Ae^{Bt+Ct^2}. \tag{1}$$

This fit is presented in Fig. 9 (together with data from other experiments) and the parameters are listed in Table III. It is a useful way to summarize the data but the exponential form lacks any fundamental theoretical significance. One must look to other formulations to gain any insight into the nature of p-p interactions. Our energies are too low to expect a Regge-pole model to be applicable. Nor do our data fit into the energy independent plot of all higher-energy p-p data suggested by Krisch.[11]

An optical model has been successfully applied to the diffraction peak which is the prominent feature of the differential cross sections at higher energies. There have been efforts made to modify the simple absorptive optical model to include the wider-angle data.[12] In our

TABLE IV. Fits to the data of the optical-model expression in Eq. (2).

P_{lab} (MeV/c)	D [mb(GeV/c)^2]	R (GeV/c)$^{-1}$	R (Fermi)
800–899	133.8 ±49.9	1.20±0.11	0.238±0.022
900–999	56.3 ±52.8	1.44±0.36	0.284±0.071
1000–1099	27.0 ±12.4	1.66±0.21	0.327±0.041
1100–1199	8.90± 2.88	2.13±0.19	0.420±0.039
1200–1299	1.92± 0.42	3.31±0.22	0.652±0.045
1300–1399	1.16± 0.08	4.03±0.11	0.794±0.021
1400–1499	0.88± 0.01	4.54±0.18	0.894±0.035
1500–1599	0.83± 0.01	4.81±0.19	0.948±0.037
1600–1699	0.70± 0.01	5.12±0.24	1.009±0.048
1700–1799	0.85± 0.01	4.81±0.19	0.948±0.039

[10] M. H. MacGregor (private communication); see also Ref. 6.
[11] A. D. Krisch, Phys. Rev. Letters **19**, 1149 (1967).
[12] T. Fujii, G. B. Chadwick, G. B. Collins, P. J. Duke, N. C. Hein, M. A. R. Kemp, and F. Turkot, Phys. Rev. **128**, 1836 (1962).

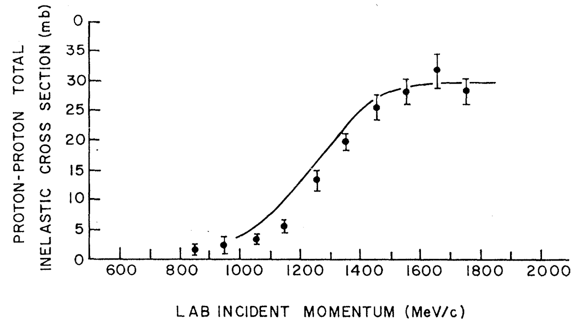

FIG. 10. Comparison between πR^2 from optical model fits to the data (see Table IV) and measured values of the total inelastic cross section (smooth curve based on data given in Refs. 2, 3, and 6).

energy region the diffraction peak is just developing so the model is of limited applicability. We have fitted our data in the diffraction region to the form

$$d\sigma/dt = \tfrac{1}{4}\pi(1+a^2-2a\cos 2\delta)R^4e^{-(R^2/4)|t|}, \tag{2}$$

which corresponds to the simple scattering amplitude

$$f(\theta) = (i/k)(1-ae^{2i\delta})J_1(kR\theta)kR/\theta,$$

where k is the wave vector of the incident proton in the c.m. system, a is the absolute amplitude of the scattered wave ($a=1$ for no absorption and $a=0$ for total absorption of the incident wave), δ is the real phase shift, R is the radius of interaction, and θ is the angle of scattering. In this model, the total inelastic cross section is given by

$$\sigma_a = (1-a^2)\pi R^2.$$

The results of fitting the data to this model are given in Table IV, with $D=1+a^2-2\cos 2\delta$. The comparison of πR^2 with the total inelastic cross section (see Fig. 10) suggests that the forward peak is indeed a diffractive effect caused by the onset of inelastic scattering.

ACKNOWLEDGMENTS

We would like to thank Professor M. G. White, Professor A. Lemonick, and Professor W. D. Wales and the staff of the Princeton-Pennsylvania Accelerator for their encouragement and cooperation. T. Droege and J. McFadden designed and built the spark-chamber readout system and computer interface. K. Wright and his staff played a major role in the construction of the wire spark chambers. J. Metzger and V. Bearg wrote a number of the programs used in this work. Excellent service was rendered by the Princeton University Computer Center, which is supported in part by National Science Foundation Grant Nos. NSF-GJ-34 and NSF-GU-3157.